Performance analysis and impedance spectral signatures of high temperature PBI–phosphoric acid gel membrane fuel cells

Nikhil H. Jalani[a], Manikandan Ramani[b], Kristina Ohlsson[c], Steve Buelte[b],
Greg Pacifico[b], Richard Pollard[b], Rhonda Staudt[b], Ravindra Datta[a,*]

[a] *Fuel Cell Center, Department of Chemical Engineering, Worcester Polytechnic Institute,*
100 Institute Road, Goddard Hall, Worcester, MA 01609, United States
[b] *Plug Power Inc., Latham, NY 12110, United States*
[c] *Royal Institute of Technology, Stockholm, Sweden*

Abstract

Polarization curves, i.e., dc performance, and impedance spectral signatures of polybenzimidazole (PBI)–phosphoric acid (H_3PO_4) membrane fuel cells are obtained in the temperature range of 160–180 °C, in an effort to investigate the effect of temperature, anode humidification, various cathode stoichs, and use of oxygen versus air. Thus, in situ electrochemical impedance spectroscopy (EIS) was used to obtain various resistances, ohmic as well as charge-transfer resistances, under these conditions. The results obtained show that PBI–H_3PO_4 gel membrane fuel cells exhibit very good performance in the temperature range of 160–180 °C with an ohmic resistance similar to Nafion. Mass transfer limitations were determined by comparing performance polarization curves with air and oxygen along with EIS. Further EIS was also used to obtain signatures during fuel starvation, and electrical shorting across the cell.
© 2006 Elsevier B.V. All rights reserved.

Keywords: Phosphoric acid; PBI; PEM; Fuel cells; Electrochemical impedance spectroscopy; Polarization

1. Introduction

Nafion-type perfluorosulfonated acid (PFSA) polymers have been widely used as a polymer electrolyte membrane (PEM) and a catalyst-binding material for electrode layers in membrane-electrode assemblies (MEAs) [1–3]. However, the conductivity of Nafion is limited by water content in the membrane and hence it cannot be used for fuel cell operations at temperatures >100 °C under atmospheric pressure. The dehydration at higher temperatures also results in membrane shrinkage and consequent poor contact between the MEA and the bipolar plates. Hence, the performance benefit arising from higher CO tolerance at higher temperatures is offset by this dehydration. There is, thus, a strong incentive to develop alternate polymer electrolytes that can work above 100 °C under low relative humidity (RH) [4].

The available polymer electrolyte membranes may be subdivided into two broad categories: (1) *proton-exchange membranes* (PEMs), e.g., Nafion, in which the acid anion is covalently attached to the polymer backbone so that only the proton is mobile, thus requiring a solvent such as water; and (2) *polymer–acid complexes* (PACs), e.g., PBI–H_3PO_4, in which the acid is simply complexed with a basic membrane so that both the proton and the anion are mobile, i.e., the transference number of protons is less than unity. While a solvent such as water is not essential for conduction in PACs, it aids by further ionizing the acid.

The development of electrolyte membranes for higher temperature operation is a particularly challenging task. A good polymer electrolyte membrane must be thin for low resistance, compliant to make a good contact with electrodes, but rigid enough to provide support to the MEA, thermally and dimensionally stable, impervious to gaseous or liquid fuels as well as electrons, durable, and should be able to provide excellent proton conductivity rivaling liquid electrolytes ($\sim$0.1 S cm^{-1}) preferably under hot and dry conditions. We have previously

---

* Corresponding author. Tel.: +1 508 831 6036; fax: +1 508 831 5853.
E-mail addresses: jalani@wpi.edu (N.H. Jalani), rdatta@wpi.edu (R. Datta).

reported on higher temperature membrane synthesis and characterization [4–6].

In the emerging family of higher temperature membranes, PBI–H_3PO_4 membranes have the potential to meet many of the requirements for higher temperature operation. PBI is an amorphous thermoplastic polymer with a glass transition temperature of 425–436 °C. It has a good chemical resistance and excellent textile fiber properties. As a membrane, PBI has so far received attention mainly for use in blood dialysis and reverse osmosis at high temperature and in harsh environments. Attempts to graft functional groups onto PBI were first made by Gieselman and Reynolds [7] and there have been persistent efforts ever since [8–24].

Chemically, PBI is a basic polymer and can readily react with acids. Wainright et al. were the first to suggest the application of acid-doped PBI based membranes for fuel cell applications [9]. Various inorganic acids have since been investigated as dopants such as H_2SO_4, H_3PO_4, $HClO_4$, HNO_3, HBr, and HCl, and organic acids like CH_3SO_3H, $C_2H_5SO_3H$, and aromatic phosphoric acids, as well as polymeric acids [9–24]. Among these various doping acids, phosphoric acid and sulphuric acid have been found to provide high conductivity. These acid moieties act both as donors and acceptors in proton transfer and therefore allow for proton migration along the anionic chain. H_3PO_4 is a particularly interesting acid due to its high conductivity and thermal stability at temperatures up to 200 °C. This is, of course, the reason for its use in phosphoric acid fuel cells.

The proton conductivity of PBI–H_3PO_4 membranes have been extensively investigated [17–28]. Other properties such as methanol crossover rate, thermal stability, water drag coefficient, mechanical properties, and kinetics of oxygen reduction have also been studied [20–24]. The PBI fuel cells have been operated at temperatures up to 200 °C without humidification of the reactant gases. At 200 °C, a PEMFC can tolerate up to 30,000 ppm CO in the reformate stream, thus enabling the elimination of CO conversion stages of the fuel processor. This opens up the possibility for a simpler, compact, and cost effective system [25–28]. This is the reason for our interest in this system.

Song et al. [29] studied the effect of electrolyte impregnation temperature, alloy catalyst, and single cell structure on electrochemical characteristics of PBI–H_3PO_4 system using EIS. They found that the high-frequency resistance of cell does not depend on acid impregnation temperature in the electrodes for fuel cells. However, they observed that the interfacial resistance of the cathode (Pt-electrolyte) increases with the increasing impregnation temperature. They further studied the effect of CO concentration and reactant gas pressure on cell performance.

The goal of this paper is to evaluate the performance of PBI–H_3PO_4 gel membranes based fuel cells for higher temperature operations. Hence, we have characterized the performance at Plug Power, Inc., in the temperature range of 160–180 °C. Since voltage of a fuel cell at a current or load in a polarization plot lumps together all types of losses, we use ac electrochemical impedance spectroscopy (EIS) for further quantifying and discriminating among the various losses. Also, it is shown in the present work that in situ EIS provides good estimate for different resistances in fuel cells that are in good agreement with

other ex-situ measurements. In addition, typical EIS signatures are identified by creating electrical shorts across a cell, during fuel starvation, and post high voltage carbon corrosion stress tests, with the objective of developing diagnostics.

2. Experimental

2.1. Fuel cell assembly and testing

Commercially available Celtec-P Series 1000 membrane–electrode assemblies from PEMEAS Fuel Cell Technologies (Frankfurt, Germany) were used in this study. Each MEA consists of a phosphoric acid electrolyte gel membrane is sandwiched between Pt catalyst based gas diffusion electrodes and supported with a polymer sub-gasket. The 44-cm^2 MEAs were compressed to a constant gap between isostatic graphite, serpentine flow-field, and gas distribution plates. In operation the membrane is approximately 0.002 in. thick. The entire single cell assembly is contained within an insulating bag, and the desired cell temperature is maintained using external pad heaters. Inlet gas temperatures were controlled through heated supply lines, and membrane humidifiers were used to control the dew point of the fuel stream. Polarization curves were obtained with hydrogen on the anode side and with air or oxygen on the cathode. Repeatability of polarization curves was confirmed with multiple polarization curves during the course of a test which also sheds light on the stability of these higher temperature fuel cells.

In summary, we studied the effect of: (1) temperature, (2) anode humidification (40–80 °C), (3) cathode flow rate (stoichs), (4) oxidant type (air and oxygen), (5) fuel starvation, and (6) induced electrical shorts across the cell. For identifying the various voltage losses within the fuel cell, electrochemical impedance spectroscopy was employed as the key characterization tool to investigate charge-transfer reaction resistance and transport resistances, including charge transport of electronic and ionic charge carriers, and mass transport through gas diffusion layer.

2.2. Electrochemical impedance spectroscopy measurements

Voltage of a fuel cell is an overall response to the current drawn, all the various internal losses being lumped within the response, which are not easy to separate with just the direct current (dc) operation. During the operation of a fuel cell, the gases are fed a at specific volumetric flow rate (standard liters per minute or slm) depending upon the current. The gases further diffuse across the gas diffusion layer (GDL) to the electrode at a rate determined by the effective diffusion coefficient of the gases in the GDL at the given temperature [30]. Once the gases reach the catalyst site, a series of reaction steps take place, some of which are chemical while others are electrochemical involving charge transfer. The rates of these reactions are also influenced by the transport of protons to or from the site. All of these individual transport and kinetic steps may be considered to have a characteristic time-constants associated with them. Electrochemical impedance spectroscopy helps separate many of these
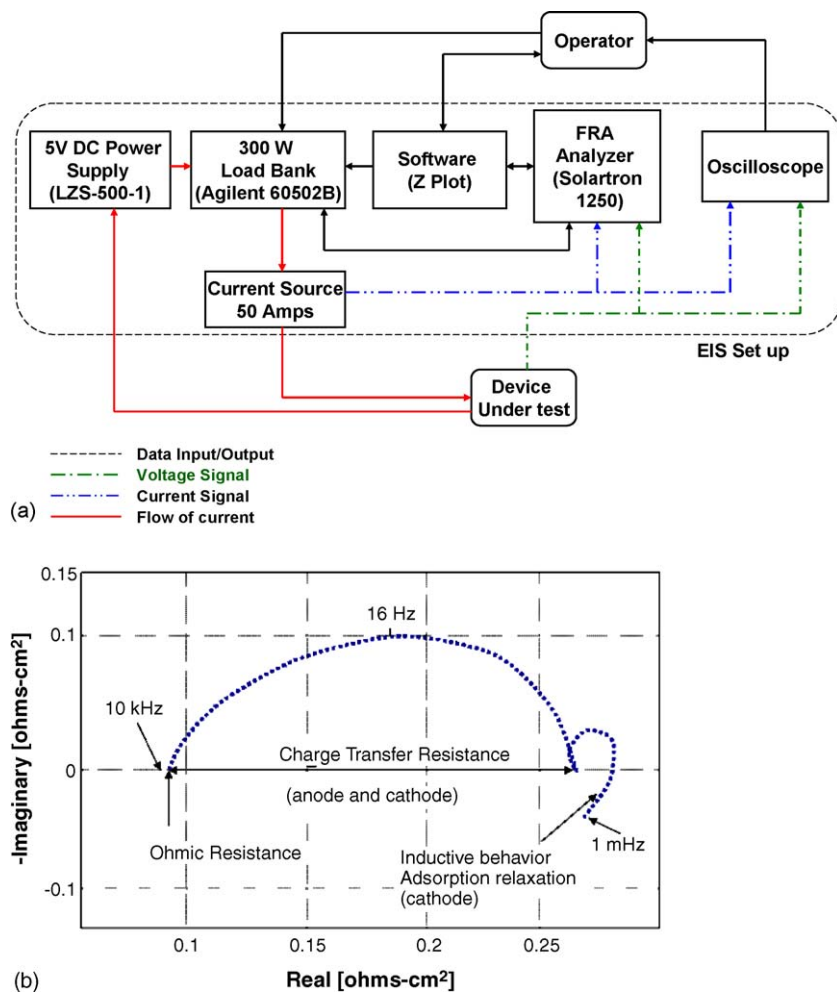
Fig. 1. (a) Electrochemical impedance spectroscopy set-up with cell interface and instrumentation interfaces. (b) Correlation between different parts of a EIS spectrum and limiting processes.

steps when a spectrum with various perturbation frequencies is employed in situ in an operating fuel cell. During our measurements, the cell was operated under a stable direct current and the perturbation amplitude was chosen making sure the system was close to linear at all current densities, especially at low and high current densities. Thus, the EIS measurements were performed with a perturbation current of 4–6% of the dc current in the frequency range 0.01 to 10^6 Hz, using a Solartron SI 1260 FRA system, obtained from Solartron. The set-up is schematically illustrated in Fig. 1(a), showing various cell interfaces with EIS instrumentation. The Solartron was interfaced with a high current interface. The Solartron generates and modulates a voltage signal to the HP load bank which in turn generates the ac current signal on top of the existing dc current.

There have been extensive studies done using EIS to characterize the working of fuel cells [31–32]. A typical EIS spectrum of a fuel cell during a frequency sweep is shown in Fig. 1(b). Both real and imaginary components of the impedance Z are plotted. The real Z-axis intercept at high frequency (i.e., intercept at the left) is assumed to provide mainly the membrane resistance, and hence, its conductivity. The low frequency intercept (on the right) is used to calculate the kinetic and mass transport resis-

tances. A brief explanation of the use of the EIS spectra to obtain various losses is discussed below.

In the higher frequency range of the spectrum, i.e., typically when the frequency is more than 10 kHz, the high-frequency intercept on the real axis in Fig. 1(b) corresponds to the ohmic resistance, R_M. Now, the overall kinetic resistance, R_P, i.e., the sum of the anodic and cathodic charge-transfer resistance, is obtained from the difference between the high-frequency real Z-axis intercept and the next lower frequency real Z-axis intercept. It is evident that the overall charge-transfer resistance R_P is dominated by the cathode impedance due to the sluggish oxygen reduction reaction (ORR) kinetics.

The lower frequency part of the spectrum, typically when frequency is less than 1 Hz, represents the sum of a capacitive loop in the anode spectrum and an inductive loop in the cathode spectrum, which appear in a similar frequency range.

The capacitive arc seen in the low frequency range can be attributed to a finite diffusion process. This is due to the mass transport in GDL and the electrode layers at anode and cathode. Because the lower frequency part of the impedance spectrum is the sum of a capacitive loop in the anode spectrum and an inductive loop in the cathode spectrum, it is not possible to

extract quantitative data from the lower frequency part of the local two-electrode spectra. It should be mentioned here that the inductive behavior seen in the high-frequency range of some of the local impedance spectra to be presented later is due to mutual inductance (i.e., cable) effects.

3. Results and discussion

3.1. Effect of temperature

The cell temperature was varied using pad heaters and the corresponding polarization curves were obtained at three different temperatures, namely of 160, 170, and 180 °C with a 55 °C dew point hydrogen on anode side and dry air on cathode side. It is well known that with an increase in temperature, the exchange current density and the conductivity of the membrane increases [30]. The dc performance of the fuel cell, thus, increased with temperature, as shown in Fig. 2(a). It can be seen that the performance of PBI–H_3PO_4 system is substantially high at higher current densities indicating that this system has a very high diffusion of oxygen in the GDL, and hence has a higher limiting current density. The good reason for this performance in PBI–H_3PO_4 fuel cell is due to the absence of liquid water in GDL because of dry air feed which keeps the pores open for effective mass transport of oxidant.

The dc performance lumps together the ohmic losses, activation losses and mass transport losses. On the other hand, EIS measurements at high frequency clearly separate ohmic resistance. These values were used in the polarization curves to obtain the cathode overpotential at different temperature assuming negligible anode overpotential. The apparent cathode Tafel slope, was thus, extracted to be about 0.105–0.11 V decade^{-1}, as shown in Fig. 2(b). The intercept values were used to extract exchange current densities at different temperatures.

The high-frequency intercepts of the Nyquist plots were compared against typical ohmic resistance values obtained from the
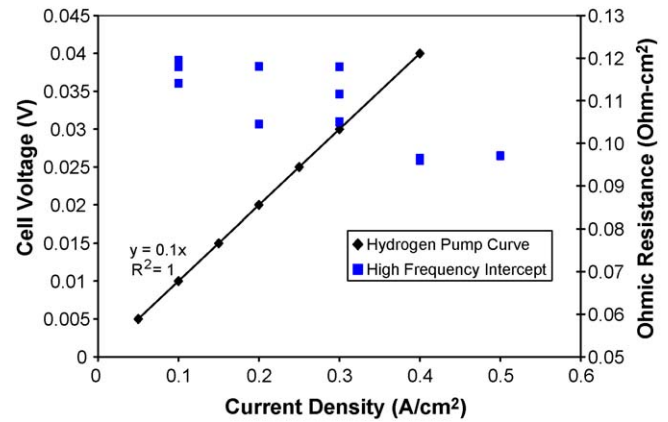

Fig. 3. Hydrogen pumping in comparison with high-frequency intercepts at 160 °C.

slope of the hydrogen pumping and were found to be similar as in Fig. 3. A scatter of around $0.02\,\Omega\,cm^2$ is seen when the EIS is performed at different current densities at 160 °C. All values at frequencies less than 1 kHz also account for additional ohmic resistance from electrolyte present in the catalyst layer.

The R_P values obtained from EIS are also plotted in Fig. 4 against current density at three different temperatures when H_2/O_2 was used. The trend of R_P declining with current density is similar at all temperatures, and the values are relatively close to each other except at higher current density of 0.3 A cm^{-2}, where a decrease in R_P with temperature is more evident.

3.2. Effect of anode dew point

Experiments described in this study were in general, performed at a constant fuel inlet dew point of 55 °C. However, the water content of the hydrogen stream could conceivably impact the performance, e.g., the high-frequency resistance via a change of the liquid H_3PO_4 electrolyte concentration within the membrane as well as the electrode layer. In order to study this effect,
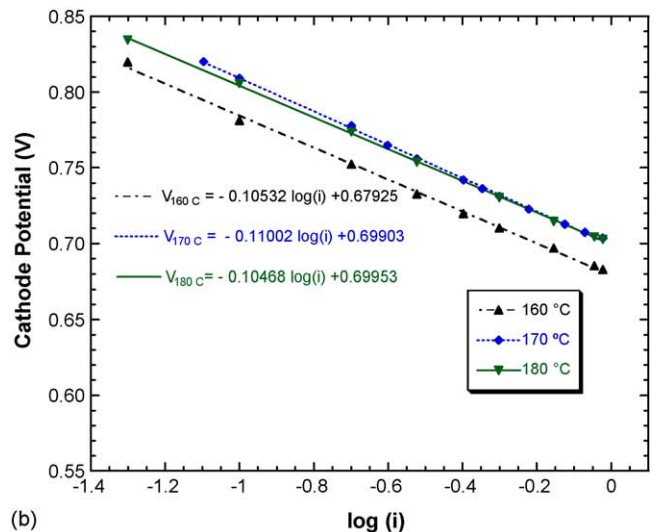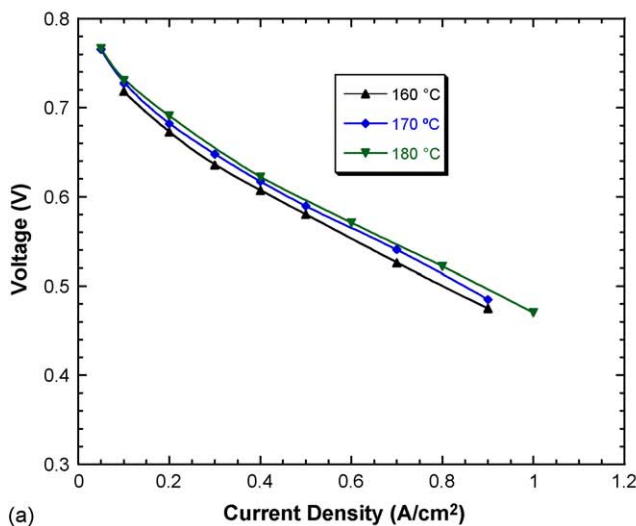

Fig. 2. (a) Polarization curves at different temperatures with air as oxidant (160–180 °C). (b) IR corrected polarization curves at different temperatures using air (160–180 °C).
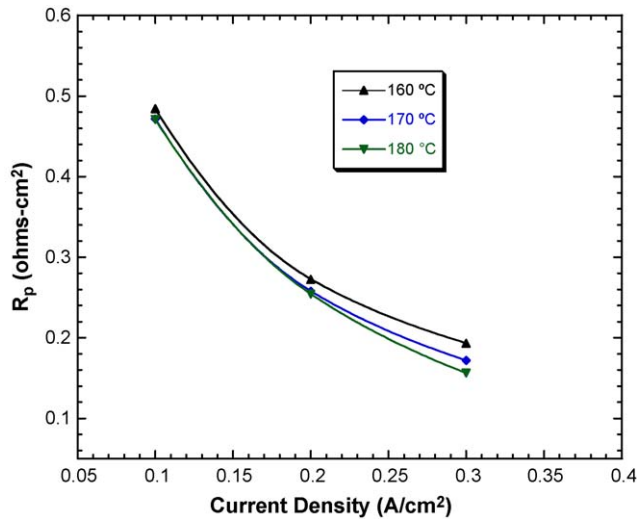
Fig. 4. Low frequency intercept as a function of current at different temperatures using oxygen as an oxidant.

polarization curves were obtained by varying the dew point of the inlet fuel stream from 40 to 80 °C at a constant cell temperature of 160 °C, as shown in Fig. 5. It can be seen that the cell performance declines somewhat with increasing anode dew point, although below 50 °C, there was little discernible difference in the polarization curves. This effect may possibly be explained by either a change in the hydrogen partial pressure as dew point increases, or due to the fact that the liquid electrolyte concentration in the membrane/electrode interfaces changes. Further experiments are needed to understand this effect in detail using EIS.

3.3. Effect of cathode stoich

Fig. 6 shows the effect of cathode stoich on the polarization curves at 160 °C. Substantial improvement in performance is seen with an increase in the cathode stoich from 1.4 to 6. These measurements indicate the onset of GDL/electrode inter-
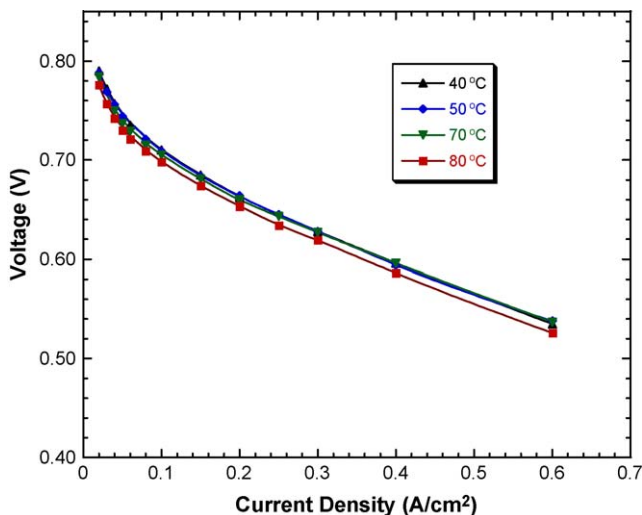

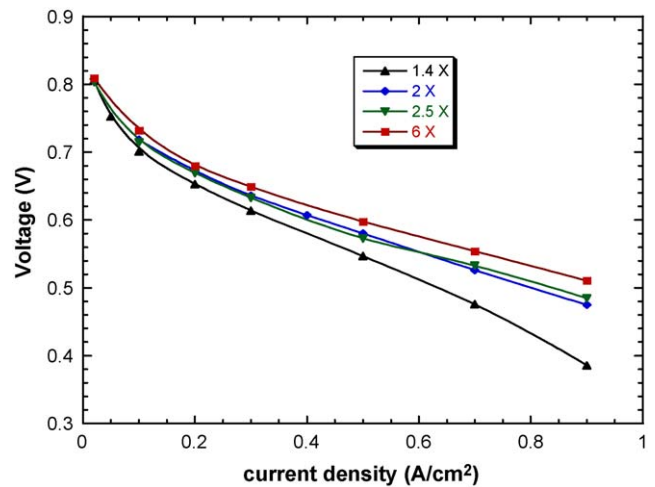Fig. 5. Effect of fuel inlet dew point temperatures on the performance curves at 160 °C.

Fig. 6. Effect of cathode stoichs on the performance curves at 160 °C.

face mass transport resistance at current densities greater than $0.2 \, A \, cm^{-2}$.

EIS was also performed to obtain R_P at multiple cathode stoichs and the results are summarized in Fig. 7 for a current density of $0.2 \, A \, cm^{-2}$ at two different temperatures. Cathode stoich clearly has a significant impact on the R_P values indicating flow channel/GDL interface mass transport resistance. With an increase in cathode stoich, the high-frequency resistance remained unaffected, but the R_P (which includes both charge transfer and diffusive losses) decreased significantly, as shown in Fig. 7, as a function of cathode flow in moles min^{-1}. In Fig. 7, a theoretical charge-transfer resistance obtained from the Tafel slope is also plotted, in order to show the deviation from theoretical even when pure oxygen is used at lower current densities. While the backpressure of the cathode chamber also increases as the air flow rate is increased; it does not contribute to substantial increase in oxygen partial pressure. However, with an increase in the cathode stoich, the log-mean or average concentration from inlet to outlet varies less significantly. Similar behavior was also observed for a current density of $0.1 \, A \, cm^{-2}$. Above $0.021 \, moles \, min^{-1}$, not much change in R_P was observed for
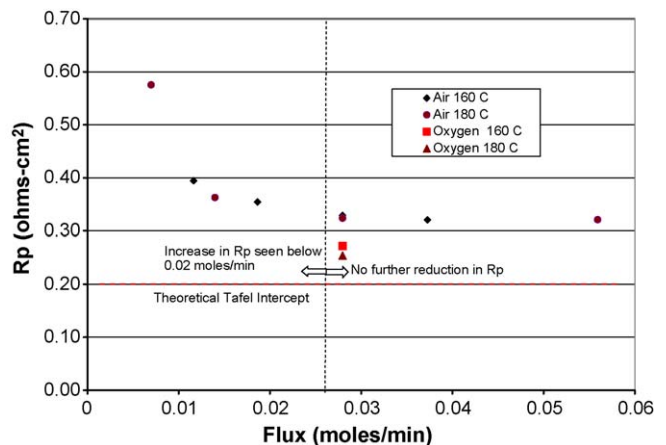

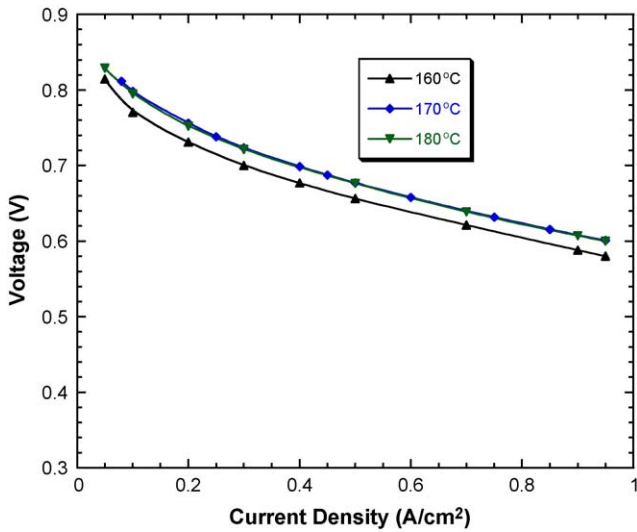Fig. 7. Low frequency intercept as a function of current density at 160 and 180 °C.

Fig. 8. Polarization curves at different temperatures with oxygen as oxidant (160–180 °C).

Fig. 10. Oxygen gain measurements at 160 and 180 °C.

$0.2\,A\,cm^{-2}$, while for $0.1\,A\,cm^{-2}$, the threshold was closer to $0.01\,moles\,min^{-1}$.

3.4. Oxygen versus air

Polarization curves and EIS parameters were also measured with air versus oxygen. Fig. 8 shows the polarization curves with oxygen at 160–180 °C. This clearly indicates that the $PBI–H_3PO_4$ system provides very good performance at higher temperatures.

The performance obtained in Fig. 9 provides the difference in the polarization curves obtained with oxygen and air. A Tafel slope of $0.1\,V\,decade^{-1}$ was obtained for oxygen curves at both 160 and 180 °C, i.e., Tafel slope is independent of temperature in this range. However, with air, even after correcting for the ohmic contribution, the resulting E versus $\log(i)$ plot showed non-linearity above $0.2\,A\,cm^{-2}$ due to diffusion limitations. Such behavior, in general, is seen in two different cases: (1) distributed ohmic resistance across the electrode and (2) mass transport limitations across the GDL. The theoretical oxygen
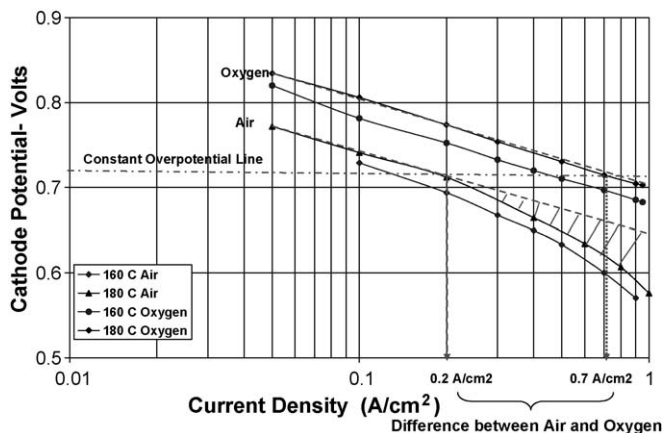

Fig. 9. Effect of oxygen concentration on polarization curves at 160 and 180 °C.
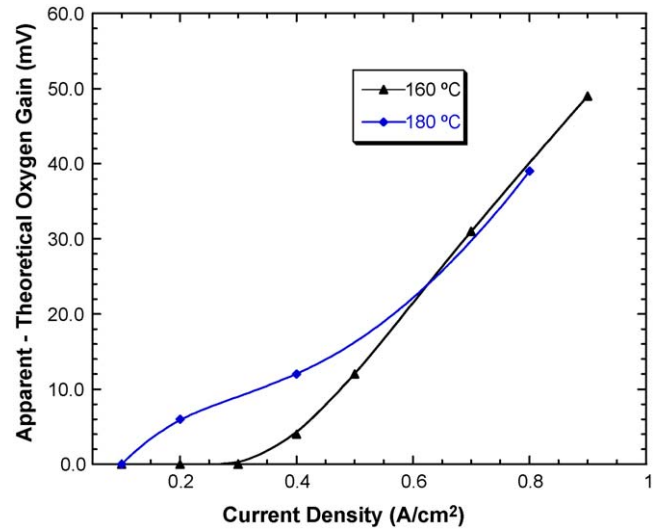
gain was calculated to be approximately 66 mV. This provides the maximum gain one could obtain if there were no diffusion limitations across the MEA.

Fig. 10 plots the deviation from this ideal gain at 160 and 180 °C as a function of current density. This clearly indicates that the mass transport across the GDL becomes significant after $0.2\,A\,cm^{-2}$ at 180 °C and at $0.4\,A\,cm^{-2}$ at 160 °C. At a constant overpotential in IR corrected polarization curves as shown in Fig. 9, the ratio of currents obtained using oxygen and air may be expected to be assumed 4 or 5, i.e., equal to the ratio of oxygen partial pressures. This is true only if the polarization curve is activation controlled and the kinetics of oxygen reduction reaction is first-order. With the polarization curve corrected for ohmic losses obtained from the 1 kHz intercept via EIS, we conclude that resulting ratio of 3.5 for currents indicates less than the theoretical. This observation begs further investigation to gain insights on the precise concentration at the electrode surface rather than the bulk feed concentration.

The R_P values were collected from EIS curves for both air and oxygen at various current densities. This enabled a comparison against theoretical R_P values obtained from known Tafel curve for oxygen, which is approximately $0.1\,V\,decade^{-1}$. The difference between measured R_P when using oxygen and air was found to be approximately $0.055–0.059\,\Omega\,cm^2$. The difference between the theoretical charge-transfer resistance from known Tafel slope and R_P using oxygen was approximately $0.059\,\Omega\,cm^2$. The IR corrected performance or the cathode potential can be expressed either as a function of current density or as a function of R_P.

The cathode potential is plotted in Fig. 11 as a function of $\log(R_P^{-1})$. Cireunnu [33] and Raistrick [34] explain the significance of using such a plot to separate charge transfer, agglomeration of catalyst particles and thin film contribution. Fig. 11 explains the relationship for both air and oxygen. This can be further used to understand the exchange current densities using air and oxygen. This shows that there might be some charge transfer and agglomeration contribution when using air at higher stoichs,
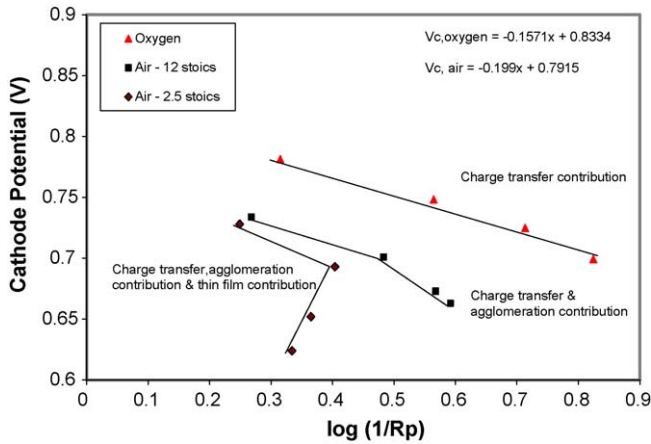
Fig. 11. Cathode potential at two concentrations of oxygen as a function of low frequency intercept at 160 °C.

whereas at lower stoichs equal to 2.5, thin film or channel/GDL contribution dominates.

3.5. Effect of fuel stoich and short circuiting

The fuel stoich was reduced by increasing the anode utilization from 70% to just over 100%. The cell was operated at 160 °C at 0.3 A cm^{-2} and a 3.6 cathode stoich during the course of this test. The cell was kept running at 1.3 anode stoich for 5 min and then reduced, while logging low frequency intercept at 0.1 Hz continuously every 5 s. As seen in Fig. 12, multiple low frequency spectrum (1 kHz–0.1 Hz) measurements were also conducted at discrete stoichs to show the onset of 45° line, which is also a characteristic of electrical short, when stoich are close to 1.0 and less. The fuel stoich shows insignificant signatures in impedance with pure hydrogen until 1.0 stoich, below which the infinite diffusion trend takes over characterized by the 45° line. At this point, the cell becomes fuel limited and the performance starts to decline at an alarming rate. In fact, the cell needs to be protected against such incidents, in general,
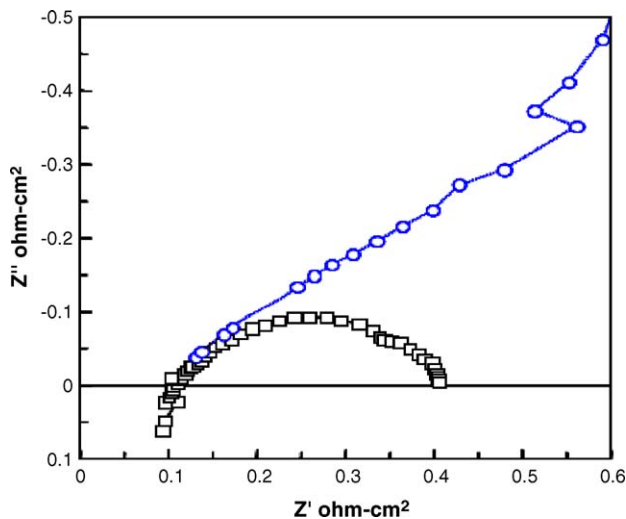

Fig. 12. EIS spectrum when fuel stoichs are lowered to close to 100% utilization at 0.3 A cm^{-2} [square: anode stoich = 1; circle: fuel starvation].
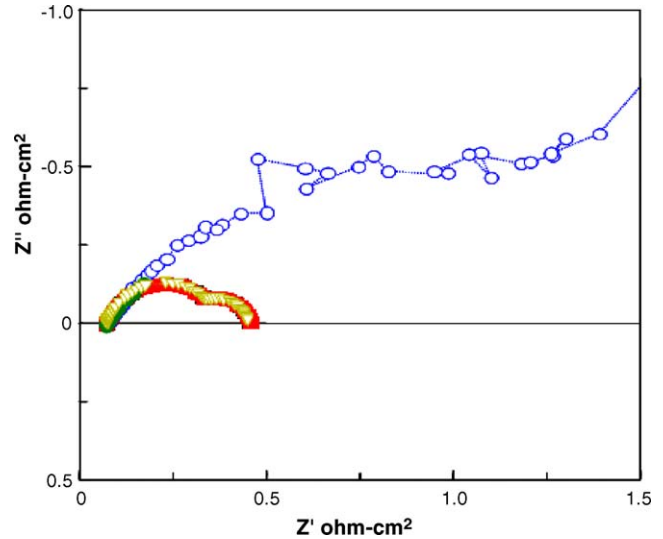

Fig. 13. EIS spectrum as cell is electrically shorted with 40 mΩ resistor [triangle: before short; square: 1 min after short; circle: 15 min after short].

since the anode potential during fuel starvation can exceed 1 V if a cell is connected to a power supply during such transients. This can irreversibly damage the anode and cathode electrode of a fuel cell limiting its life. This impedance signature can, thus, show the trend before cell performance starts to decline and can be used to control then fuel cells more pro-actively.

The cell was also electrically shorted with a 40 mΩ resistor, while operating at 180 °C at 0.219 A cm^{-2} with 1.5 fuel stoich and 2 air stoich. During this measurement, the cell experienced increased net current due to two parallel current demands—one from the load bank and the other through the shorted electrical resistor. At this point, as seen in Fig. 13, the 45° line starts to take over at 25 Hz with the short applied across the cell. This signature is similar to the fuel starvation signature, however in this case; one or both electrodes may be starved of reactants. Increasing both the fuel and air stoichs resulted in normal behavior after the increased current demand was met by the increased fuel and air flow rates. However, the 3–20 Hz lobe is reduced post shorting since additional current is being drawn.

4. Conclusions

It has been demonstrated that the PEMEAS PBI–phosphoric acid based MEAs provide very good performance in the operating temperature range of 160–180 °C. The high-frequency intercept in EIS experiments indicate an ohmic contribution of about 0.1 Ω cm^2, which is similar to that for Nafion membrane under fully humidified conditions at 80 °C. Performance was investigated at various fuel inlet dew points and it was found that an increase in dew point somewhat affects the performance of the PBI system. By varying cathode stoich, the observed change in performance and impedance behavior indicates that variation of oxygen partial pressure from inlet to outlet of a fuel cell have a profound effect on measured global responses in voltage and impedance. Comparing polarization curves with air and oxygen, it is apparent that the diffusive losses exist across the GDL. Diffu-

sion losses quantified at two different temperatures indicate that there are significant diffusion losses at current densities greater than 0.4 A cm^{-2}. Two extreme cases of reactant starvation were studied using fuel starvation and electrically shorting the cell. Impedance signatures developed during fuel starvation shows a 45° line and this signature is similar when a cell is electrically shorted.

Acknowledgements

References

[1] K.D. Kreuer, J. Membr. Sci. 185 (2001) 29.
[2] A.J. Appleby, F.R. Foulkes, Fuel Cell Handbook, Van Nostrand Reinhold, New York, 1989.
[3] M. Doyle, M.E. Lewittes, M.G. Roelofs, S.A. Perusich, J. Phys. Chem. B 105 (2001) 9387.
[4] N.H. Jalani, K. Dunn, R. Datta, Electrochim. Acta 51 (3) (2005) 553.
[5] N.H. Jalani, R. Datta, J. Membr. Sci. 264 (1–2) (2005) 167.
[6] N.H. Jalani, P. Choi, R. Datta, J. Membr. Sci. 254 (1–2) (2005) 31.
[7] M.B. Gieselman, J.R. Reynolds, Macromolecules 26 (1993) 5633.
[8] P. Staiti, F. Lufrano, A.S. Arico', E. Passalacqua, V. Antonucci, J. Membr. Sci. 188 (2001) 71.
[9] J.S. Wainright, J.-T. Wang, D. Weng, R.F. Savinell, M. Litt, J. Electrochem. Soc. 142 (1995) L121.
[10] G. Xiao, Q. Li, H.A. Hjuler, R.W. Berg, N.J. Bjerrum, J. Electrochem. Soc. 142 (1995) 2890.
[11] Q. Li, R. He, J.O. Jensen, N.J. Bjerrum, Chem. Mater. 15 (2003) 4896.
[12] P. Staiti, M. Minutoli, J. Power Sources 94 (1) (2001) 9.
[13] J.S. Wainright, M.H. Litt, R.F. Savinell, in: W. Vielstichm, A. Lamm, H.A. Gasteiger (Eds.), Handbook of Fuel Cells, 3, John Wiley & Sons Ltd., 2003, p. 436.
[14] Q. Li, R. He, J.O. Jensen, N.J. Bjerrum, Fuel Cells Fundam. Syst. 4 (2004) 147.
[15] X. Glipa, M.E. Hadda, D.J. Jones, J. Roziere, Solid State Ionics 145 (1997) 61.
[16] R. Bouchet, E. Siebert, Solid State Ionics 118 (1999) 287.
[17] X. Glipa, B. Bonnet, B. Mula, D.J. Jones, J. Roziere, J. Mater. Chem. 9 (1999) 3045.
[18] B. Xing, O. Savadogo, J. New Mater. Electrochem. Syst. 2 (1999) 95.
[19] M. Kawahara, J. Morita, M. Rikukawa, K. Sanui, N. Ogata, Electrochim. Acta 45 (2000) 1395.
[20] Q. Li, H.A. Hjuler, N.J. Bjerrum, J. Appl. Electrochem. 31 (2001) 773.
[21] J.J. Fontanella, M.C. Wintersgill, J.S. Wainright, R.F. Savinell, M. Litt, Electrochim. Acta 43 (1998) 1289.
[22] H. Pu, W.H. Meyer, G. Wegner, J. Polym. Sci., Part B, Polym. Phys. 40 (2002) 663.
[23] H. Akita, M. Ichikawa, K. Nosaki, H. Oyanagi, M. Iguchi, U.S. Patent 6 124 060 (2000).
[24] J.A. Kerres, J. Membr. Sci. 185 (2001) 3.
[25] Q. Li, R. He, J. Gao, J.O. Jensen, N.J. Bjerrum, J. Electrochem. Soc. 150 (2003) A1599.
[26] R. He, Q. Li, G. Xiao, N.J. Bjerrum, J. Membr. Sci. 226 (2003) 169.
[27] D. Cheddie, N. Munroe, Energy Convers. Manage. 47 (11–12) (2006) 1490.
[28] Q. Li, H.A. Hjuler, C. Hasiotis, C.G. Kontoyannis, N.J. Bjerrum, Electrochem. Solid State Lett. 5 (2002) 125.
[29] R.H. Song, D.J. Kim, C.S. Kim, D.R. Shin, J. New Mater. Electrochem. Syst. 4 (2001) 47.
[30] T. Thampan, N.H. Jalani, P. Choi, R. Datta, J. Electrochem. Soc. 152 (2) (2005) A316.
[31] I.A. Schneider, H. Kuhn, A. Wokaun, G.G. Scherer, J. Electrochem. Soc. 152 (2005) A2092.
[32] O. Antoine, Y. Bultel, R. Durand, J. Electroanal. Chem. 499 (2001) 85.
[33] M. Ciureanu, J. Phys. Chem., B 105 (2001) 3531.
[34] I.D. Raistrick, Electrochim. Acta 35 (1990) 1579.